RESEARCH ARTICLE | APRIL 15 2026

Impact of NMC 811 electrode porosity on GHz burst laser ablation characteristics

Special Collection: Advanced Laser Technology and Its Applications

Niclas Straßburger ; Penghui Zhu ; Wilhelm Pfleging

J. Laser Appl. 38, 022020 (2026)
https://doi.org/10.2351/7.0002070

Journal of Laser Applications ARTICLE pubs.aip.org/lia/jla

Impact of NMC 811 electrode porosity on GHz burst laser ablation characteristics

Cite as: J. Laser Appl. 38, 022020 (2026); doi: 10.2351/7.0002070
Submitted: 30 December 2025 · Accepted: 27 March 2026 ·
Published Online: 15 April 2026

Niclas Straßburger,[a] Penghui Zhu, and Wilhelm Pfleging

AFFILIATIONS

Karlsruhe Institute of Technology, IAM-AWP, Kaiserstraße 12, Karlsruhe 76131, Germany

Note: This paper is part of the Special Topic on Laser Manufacturing for Future Mobility.
[a]**Author to whom correspondence should be addressed; electronic mail:** niclas.strassburger@kit.edu

ABSTRACT

Significant improvements in lithium-ion battery performance such as lifetime, fast charging, and high-power capability can be achieved by using three-dimensional (3D) electrode architectures in comparison to state-of-the-art two-dimensional (2D) electrodes. To establish such an advanced 3D electrode concept, high-power ultrafast laser ablation has proven to be a precise and efficient approach. The production of 3D electrodes with laser ablation needs to be integrated into an already established and complex processing chain for battery production. This requires efficient coordination and harmonization of these processing steps with regard to diverse aspects in electrode manufacturing such as the selected composite material system, its targeted micro- and nano-structures, processing speed, and process reliability. In particular, electrode calendering is an established processing step, which holds great importance as it has a significant impact on the structural properties of the electrode on the micro- and nano-scale, including porosity, composite density, and layer cohesion and adhesion to the current collector. In this study, the impact of laser structuring using GHz bursts on $LiNi_{0.8}Mn_{0.1}Co_{0.1}O_2$ (NMC 811) cathodes with porosities between 10% and 40% is investigated. Distinct ablation characteristics are observed depending on electrode porosity and laser burst length, revealing a clear interplay between both parameters. Shorter bursts significantly increase ablation efficiency for electrodes with higher porosities, whereas for lower porosities, ablation efficiency is higher for longer bursts. Morphological analysis shows that shorter burst lengths lead to minor visible modification, indicating that the ablation process is dominated by binder removal. In contrast, longer burst lengths produce more homogeneous, layer-like surface structures, suggesting an additional temperature-driven contribution due to cumulative heating effects. A processing rate of 1.67 cm^2/s is achieved for a burst length of 500 ns at a burst fluence of 20.2 J/cm^2, demonstrating the potential for industrial upscaling, for example, by using higher laser power in combination with beam splitting. These results highlight the potential of GHz burst laser ablation for the structuring of 3D lithium-ion battery electrodes and provide a basis for further process optimization.

Key words: 3D battery, GHz laser ablation, ultrafast laser structuring, porosity, NMC 811, lithium-ion battery

I. INTRODUCTION

To meet evolving energy storage demands, continuous advancements in battery technology are required. Lithium-ion batteries (LIBs) have established themselves as the dominant energy storage solution due to their superior energy and power density, making them particularly suitable for applications such as electric vehicles.[1] The need to further enhance LIB performance has driven research into active materials with high energy density, fabrication of thick-film electrodes, and novel electrode architectures.[2]

High-energy electrode materials, combined with thick-film electrodes exceeding thicknesses beyond 100 μm, have enabled commercial LIBs to achieve energy densities of over 700 Wh/l and 250–300 Wh/kg at the cell level.[3] This translates to battery-electric vehicles achieving driving ranges of up to 450–550 km in the long-range WLTP, which is comparable to those of vehicles with an internal combustion engine.[3] However, challenges persist in optimizing the trade-off between energy density, power output, manufacturing reliability, and cost-effectiveness.[2–4]

Beyond material development, further optimization can be achieved through advanced electrode design.[2,5–9] Increasing electrode mass loading, integrating three-dimensional (3D) electrode structures, and transferring these advancements to large-scale production are key strategies for improving LIB performance.[2,5–9] Laser structuring has emerged as a viable approach to establish the 3D battery concept by introducing micro- and sub-micrometer modifications that enhance the battery performance.[5–9] Various structured designs, including line, grid, and hole patterns, have been shown to mitigate mechanical degradation, improve electrolyte wettability, enhance charge transport, and reduce lithium plating risks at higher current densities.[5–9] High-power ultrafast laser ablation is a precise and effective technique for fabricating such structures, but its integration with traditional high-throughput battery manufacturing processes remains open due to the necessity of an upscaled and robust process.[5–10]

One promising technology to improve the processing speed of laser ablation, and as a result the upscaling of this process, is the GHz laser ablation, which increases the process efficiency significantly compared to MHz and single-pulse laser ablation.[11–14] In addition to these scaling challenges, adopting laser structuring as a novel modification to established processes raises new optimization questions. One of these established manufacturing steps is the calendering step in LIB production, which significantly affects the microstructural characteristics of the electrode, including porosity, electronic conductivity, density, wettability, and adhesion strength of the composite electrode to the current collector.[15–18]

Understanding the interplay between the laser ablation process and the electrode density, which is mainly controlled by particle size distribution and the calendering process, is essential for optimizing the 3D battery concept. This is not only important for the performance of the LIB, but also for optimizing the laser ablation efficiency itself. To address this current research gap, this study investigates the effects of varying GHz burst laser ablation parameters on $LiNi_{0.8}Mn_{0.1}Co_{0.1}O_2$ (NMC 811) electrodes, which were calendered to different levels of porosity ranging from 10% to 40%. This approach leads to the identification of distinct ablation characteristics based on porosity and burst length, revealing clear trends in the interplay between these parameters.

II. EXPERIMENT

A. Electrode manufacturing

NMC 811-based electrodes were prepared by mixing polycrystalline NMC 811 powder with a median particle size of 9.34 μm (S85E, Gelon Lib Group Co. Ltd, Shandong, China), conductive carbon additives, including carbon black (SC65, C-NERGY SUPER C65, Imerys S.A., Paris, France) and conductive graphite (KS6L, C-NERGY KS 6L, Imerys S.A., Paris, France). Polyvinylidene fluoride (PVDF, Solef 5130, Solvay S.A., Brussels, Belgium) binder was priorly dissolved in N-methyl-2-pyrrolidone (NMP, Merck KGaA, Darmstadt, Germany). Table I shows the corresponding weight percentages of the aforementioned materials. The binder solution was prepared at a weight ratio of 1:10 (PVDF:NMP). The binder solution and the subsequent NMC 811 slurry were homogenized in a centrifugal mixer (SpeedMixer DAC 150 SP, Hauschild GmbH & Co. KG, Hamm, Germany). The slurry was coated onto aluminum foil with a thickness of 20 μm using a doctor blade (ZUA 2000.100, Screening Eagle Technologies AG, Schwerzenbach, Switzerland) on a laboratory coater (MSK-AFA-IV, MTI Corporation, Richmond, USA) and dried at 90 °C for 2 h.

TABLE I. Material and mass fraction of each component in the NMC 811 slurry.

Material	Mass fraction (wt. %)
NMC 811	92
SC65	3
KS6L	2
PVDF	3

The NMC 811 electrodes were subsequently calendered at 50 °C using a precision rolling press (HR01, MTI Corporation, Richmond, USA) to achieve porosities ranging from 10% to 40%. Film thicknesses were measured using a digital gauge (Millimess 2000 W, Mahr GmbH, Göttingen, Germany) at five positions across the width and three along the length to ensure consistency.

B. Laser structuring of electrodes

A high-power GHz burst laser (PXpv, EdgeWave GmbH, Würselen, Germany) integrated into a laser micromachining system (MSV203 Laser Patterning Tool, M-SOLV Ltd., Oxford, UK) was used for the laser structuring of NMC 811 electrodes. The laser was operated at a wavelength (λ) (nm) of 1064 nm with a maximum average laser power (P_{avg}) (W) of 450 W and a pulse duration (τ_{pulse}) (ps) of 10 ps. The laser pulse repetition rate ($f_{rep,pulse}$) (GHz) within a burst was set to 0.5 GHz, while the burst repetition rate ($f_{rep,burst}$) (MHz) can be increased up to 1 MHz, and the burst length (τ_{burst}) (ns) can be adjusted from 30 to 500 ns. Figure 1 illustrates the difference between the pulse repetition rate and the burst repetition rate.

Line patterns were structured using an average laser power ranging from 1 to 10 W at a burst repetition rate of 100 kHz and 10 to 100 W at 1 MHz. The laser scan speed (v_{scan}) (m/s) was set to 2 m/s at a burst repetition rate of 100 kHz and 20 m/s at 1 MHz. This results in a pulse-to-pulse distance ($x_{pulse\text{-}to\text{-}pulse}$) ($\mu$m) of

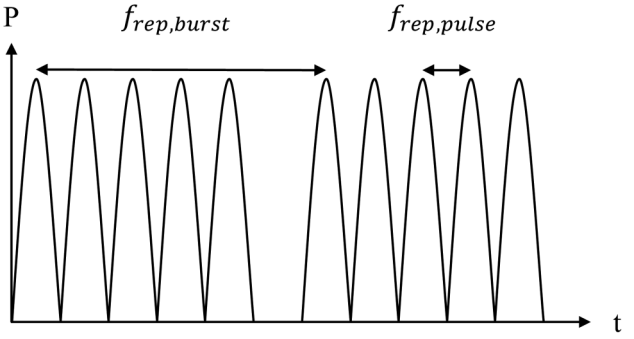

FIG. 1. Schematic illustration of laser pulse repetition rate ($f_{rep,pulse}$) within a burst and burst repetition rate ($f_{rep,burst}$) plotted over time (t) and power (P).

TABLE II. Setups used to investigate the ablation behavior with variations in the burst length (τ_{burst}), burst repetition rate ($f_{rep,burst}$), and scan speed (v_{scan}) resulting in the same pulse-to-pulse distance and burst energy (E_{burst}).

Setup	1	2	3	4
τ_{burst} (ns)	50	500	50	500
$f_{rep,burst}$ (kHz)	100	100	1000	1000
v_{scan} (m/s)	2	2	20	20

20 μm, with a calculated mean beam waist of 11 μm. For each set of laser parameters, three scan repetitions (n_{scan}) (-) were performed across five parallel lines with a pitch (x_{pitch}) (μm) of 200 μm. The setups presented in Table II were used to investigate the ablation behavior by varying the burst length and burst repetition rate with the same pulse-to-pulse distance and burst energy (E_{burst}) (J). The energy delivered per burst is determined by the average laser power and the burst repetition rate, using Eq. (1). With a train of identical pulses, we assume the burst energy is related to the standard pulsed-laser energy-power relations,

$$E_{burst} = \frac{P_{avg}}{f_{rep,burst}}. \quad (1)$$

The burst length was set to 50 and 500 ns to explore a transition from less temperature-driven to more temperature-driven ablation regimes. With a burst repetition rate of 0.5 GHz (i.e., a pulse-to-pulse interval of 2 ns in space-time), 25 and 250 pulses are used in a single burst to study the impact on the ablation behavior of NMC 811 electrodes.

In addition, the average laser power was varied in order to study the impact of the laser burst fluence (F_{burst}) (J/cm^2) on the laser ablation behavior and to determine optimal ablation conditions for NMC 811 electrodes as a function of porosity. Assuming a Gaussian beam profile, the burst fluence is determined by the average laser power, the burst repetition rate, and the beam radius, using Eq. (2),

$$F_{burst} = \frac{2 \cdot P_{avg}}{f_{rep,burst} \cdot \omega_0^2 \cdot \pi}. \quad (2)$$

Due to a slightly elliptical Gaussian, a ω_{0X} of 0.00126 cm and a ω_{0Y} of 0.001 cm were used to calculate ω_0^2. This method was explained in detail by Ledesma *et al.*[19] The corresponding results are listed in Table III.

III. RESULTS AND DISCUSSION

A. Electrode preparation

The initial film thickness (without the current collector) of the NMC 811 cathodes before calendering was 97.9 ± 1.0 μm with an active mass loading of 20.82 mg/cm^2 and an areal capacity of 3.58 mAh/cm^2. Table IV presents details related to the film thickness and achieved porosity of the NMC 811 electrodes used in this study. For each porosity, the table delineates the variations in film thickness and correlates these measurements with the respective calculated porosities achieved through the calendering process. The porosity values of the NMC 811 cathodes were determined by weighing the samples and then calculated using the weight percentage and density of each component in the electrode. This method was explained in detail by Zhu *et al.*[20] In the calendering process, the measured variable is the layer thickness. The porosity is then calculated under the assumption of constant mass loading, and under the same assumption the electrode density is also calculated. Uncertainties in porosity and density result from deviations in determining the layer thickness. Any possible changes in mass loading (e.g., displacement of the current collector or the layer material) were neglected. For the purpose of better distinction, the porosities 28% and 18% were later referred to as their approximated values of 30% and 20%, respectively.

TABLE III. Used average laser power (P_{avg}) at the burst repetition rate ($f_{rep,burst}$) of 100 kHz and 1 MHz, as well as the resulting laser burst fluences (F_{burst}).

P_{avg} (W) ($f_{rep,burst}$ = 100 kHz)	P_{avg} (W) ($f_{rep,burst}$ = 1 MHz)	F_{burst} (J/cm^2)
1	10	5.1
2	20	10.1
4	40	20.2
6	60	30.3
8	80	40.4
10	100	50.5

In addition to the film thickness measurement, the electrodes were examined using an optical microscope (Reichert-Jung MeF3, Danaher Corporation, Washington, DC, USA) at an optical magnification of 50. Figure 2 shows a decrease in film thickness from 87.5 to 58.5 μm and a corresponding reduction in calculated electrode porosity from 40% to 10%. Additionally, it shows a slight current collector thinning (up to 2 μm) as well as particles pressed into the current collector of the NMC 811 electrodes when the porosity was below 30%. The indentation of NMC 811 particles in the current collector is marked with blue arrows in Figs. 2(b)–2(d).

B. Laser structuring of the NMC 811 electrodes

Figure 3 introduces three parameters relevant for further evaluation—the ablated area (μm^2) and ablated depth (μm), as well as the ablated full width at half maximum (FWHM) (μm), which are illustrated using an example of a structure in NMC cathodes.

TABLE IV. Achieved film thicknesses, calculated porosities, and calculated density of the NMC 811 electrodes after calendering.

Film thickness (μm)	Calculated porosity (%)	Calculated density (g/cm^3)
97.9 ± 1.0	46.3 ± 0.6	2.31 ± 0.02
87.5 ± 0.9	40.0 ± 0.6	2.59 ± 0.03
72.9 ± 0.4	28.0 (30) ± 0.4	3.10 ± 0.01
64.4 ± 0.7	18.5 (20) ± 0.8	3.51 ± 0.03
58.5 ± 0.5	10.2 ± 0.8	3.87 ± 0.03

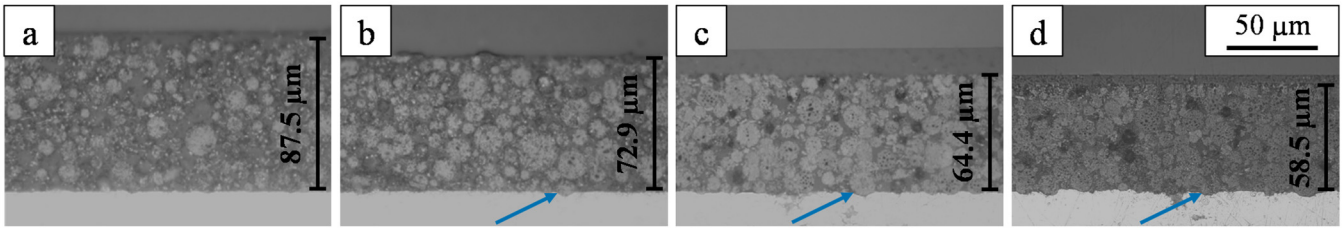

FIG. 2. Cross-sectional views of NMC 811 electrodes. Different film thicknesses and porosities of 40% and 30% were shown in (a) and (b), respectively, as well as electrodes with 20% and 10% porosities represented in (c) and (d), respectively. With lower porosities, particles are pressed into the current collector, marked with blue arrows in (b)–(d).

The line patterns of the laser-structured cathodes were analyzed using a digital microscope (VHX-7000, Keyence Corporation, Osaka, Japan) to obtain the data shown in Figs. 4 through 9. The analyzed patterns represent an average of 11 profiles with a profile distance of 30 μm. In Fig. 4, the ablated area is plotted versus the corresponding burst repetition rate at 100 kHz and 1 MHz. The data points in blue and green present the ablation of the high porosity electrodes with 40% and 30%, while the low-porosity electrodes are displayed in orange and purple for 20% and 10%, respectively. Additionally, the results for a burst length of 50 ns are shown with squares and solid lines, while the results for a burst length of 500 ns are shown with triangles and dotted lines. This design scheme is also used in Figs. 4 through 9.

As shown in Fig. 4, the ablated area increased with higher burst fluences over the full studied burst fluence range of 5.1–50.5 J/cm^2. At higher porosities (green and blue), the shorter burst length (squares) led to more material ablation, i.e., an increasing ablated area was observed. At lower porosities (purple and orange), longer burst lengths (triangles) resulted in more material removal. In addition, the standard deviation increases for higher porosities. When comparing Fig. 4(a) with Fig. 4(b), only a minor difference toward marginally more uniform curves using a 100 kHz burst repetition rate and a smaller gap between the two burst lengths is visible, e.g., by comparing the blue solid lines and blue dotted lines.

To compare ablation performance across different parameter sets, the laser ablation efficiency (*Eff*) (mm^3/J) is introduced, following the standardized use of ablation efficiency as ablated volume per energy, and determined by the ablated area, the scan speed, the average laser power, and the scan repetitions, using Eq. (3),

$$Eff = \frac{\text{area} \cdot v_{\text{scan}}}{P_{\text{avg}} \cdot n_{\text{scan}}}. \tag{3}$$

This calculation allows the evaluation of the process efficiency. Figure 5 presents the ablation efficiency versus the burst fluence; here similar trends to those in Fig. 4 are shown with shorter burst lengths (squares) ablating material more efficiently at higher porosities (green and blue), while longer burst lengths increase the efficiency at lower porosities (purple and orange). The ablation efficiency increases with higher burst fluences over the full range of 5.1–50.5 J/cm^2. In addition, the standard deviation increases for higher porosities and the higher value at 5.1 J/cm^2 is likely to be caused by an ablation threshold that requires further analysis but is not discussed further in this work. When comparing Fig. 5(a) with Fig. 5(b), a smaller gap between the two burst lengths, comparing green solid lines and green dotted lines, as well as blue solid lines and blue dotted lines, is again visible. Additionally, a minor difference toward more uniform curves using a 100 kHz burst repetition rate is again recognizable.

While the ablation efficiency value is a useful indicator for upscaling, structures with optimal geometries must also be taken into consideration. It would be most beneficial for optimizing the battery performance and minimizing the active mass loss if the laser generated structures are extended close to the current collector while remaining as narrow as possible. This helps prevent excessive ablation of the active material NMC 811, thereby avoiding unnecessary capacity reduction, while keeping the potential benefits of the 3D battery concept. For this purpose, the *aspect ratio* is considered and determined by the ablated depth and the ablated FWHM, using Eq. (4),

$$\text{Aspect ratio} = \frac{\text{Depth}}{FWHM}. \tag{4}$$

The *aspect ratio* (—) is shown in Fig. 6, where a clear trend for longer burst lengths achieving higher *aspect ratios* is recognizable for all porosities. The *aspect ratio* increases with higher burst

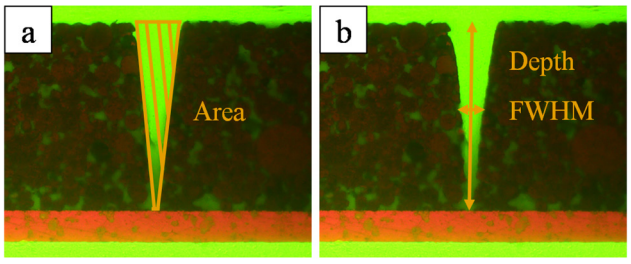

FIG. 3. Cross-sectional views of an NMC electrode with markings for the relevant parameters of the ablated area [represented in (a)] and ablated depth as well as ablated FWHM [represented in (b)].

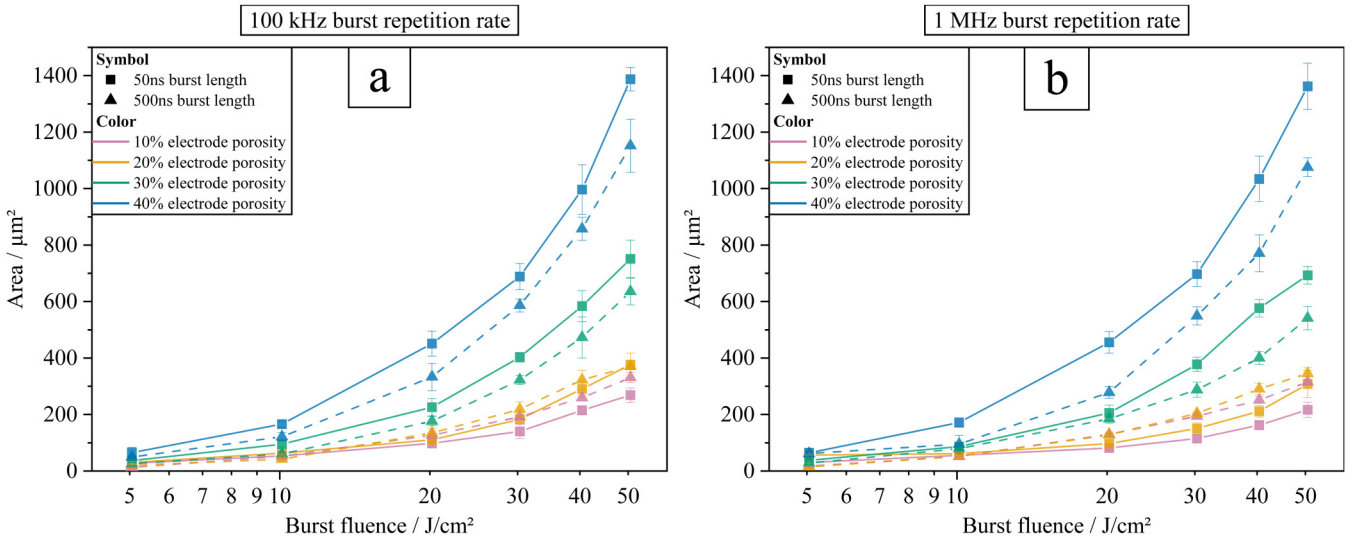

FIG. 4. Ablated area as a function of burst fluence (F_{burst}) with a burst repetition rate ($f_{rep,burst}$) of 100 kHz (a) and 1 MHz (b) and values for 50 ns (square) and 500 ns (triangle) burst length (τ_{burst}) as well as 40% (blue), 30% (green), 20% (orange), and 10% (purple) porosity.

fluences over the full range of 5.1–50.5 J/cm^2. In addition, the standard deviation increases again for higher porosities (green and blue). When comparing Fig. 6(a) with Fig. 6(b), only a minor difference toward more uniform curves using a 100 kHz burst repetition rate and a faster rising curve for the ablation of the high-porosity electrode is visible, by comparing blue solid lines and blue dotted lines.

The *aspect ratio* is typically used in laser ablation processes and will now be further analyzed by its components—the depth and FWHM—for a more detailed understanding of the influences of burst fluence on the channel geometry. Figure 7 illustrates similar ablation scenarios for NMC 811 electrodes with lower (purple and orange) and higher porosities (green and blue), as well as for shorter and longer burst lengths, where the ablation depth

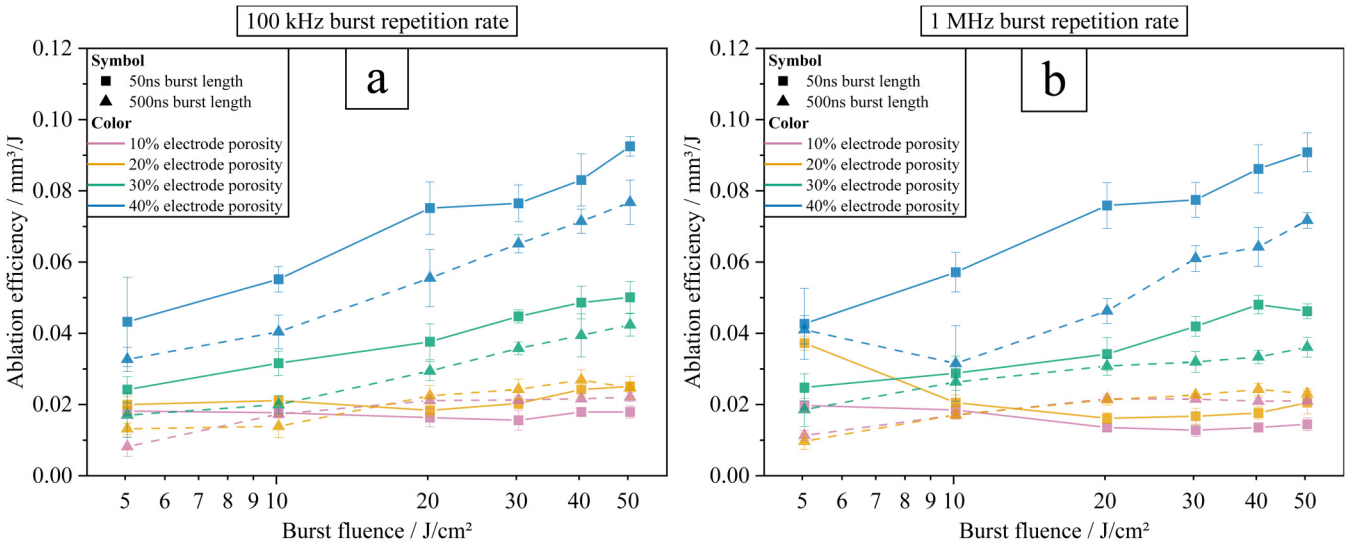

FIG. 5. Ablation efficiency (*Eff*) as a function of burst fluence (F_{burst}) with a burst repetition rate ($f_{rep,burst}$) of 100 kHz (a) and 1 MHz (b) and values for 50 ns (square) and 500 ns (triangle) burst length (τ_{burst}) as well as 40% (blue), 30% (green), 20% (orange), and 10% (purple) porosity.

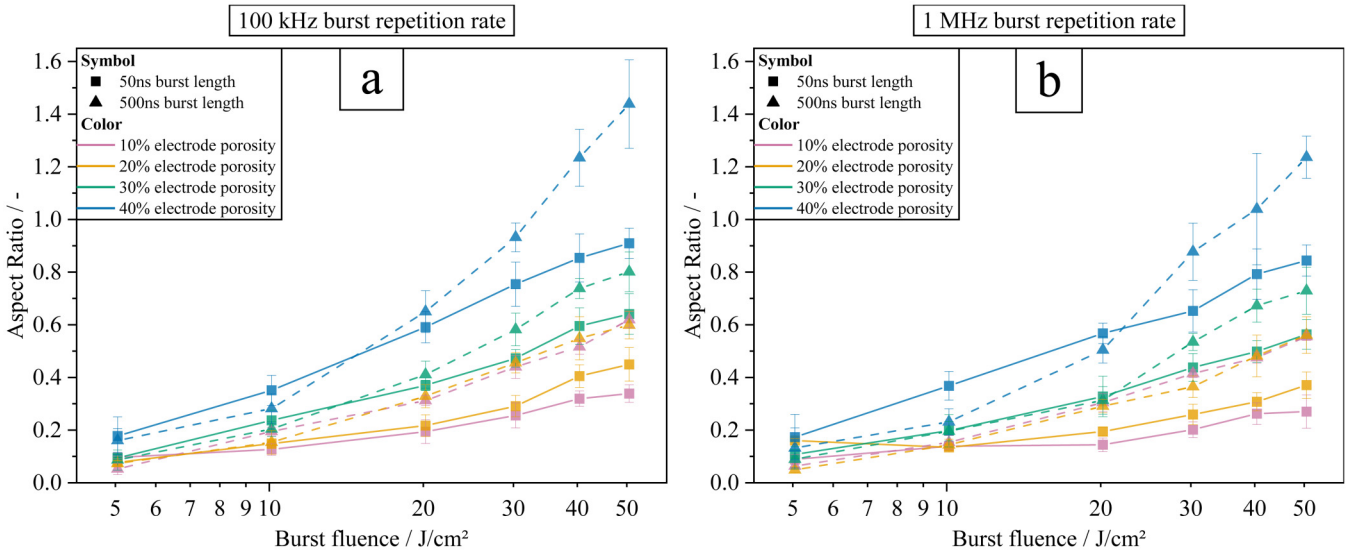

FIG. 6. *Aspect ratio* as a function of burst fluence (F_{burst}) with a burst repetition rate ($f_{rep,burst}$) of 100 kHz (a) and 1 MHz (b) and values for 50 ns (square) and 500 ns (triangle) burst length (τ_{burst}) as well as 40% (blue), 30% (green), 20% (orange), and 10% (purple) porosity.

increases with higher burst fluences over the full range of 5.1–50.5 J/cm^2. In addition, the standard deviation increases for higher porosities. When comparing Fig. 7(a) with Fig. 7(b), the gap between the two burst lengths for high porosities and a minor difference toward more uniform curves using a 100 kHz burst repetition rate is again visible, e.g., by comparing blue solid and blue dotted lines.

Figure 8 shows the FWHM, which presents a clear trend of longer burst lengths leading to smaller FWHM values. This clarifies that the *aspect ratio* trend is significantly and positively influenced by the contribution of the ablated width. The FWHM increases with higher burst fluences over the full investigated burst fluence range of 5.1–50.5 J/cm^2. In addition, the standard deviation increases for higher porosities (green and blue), while the higher

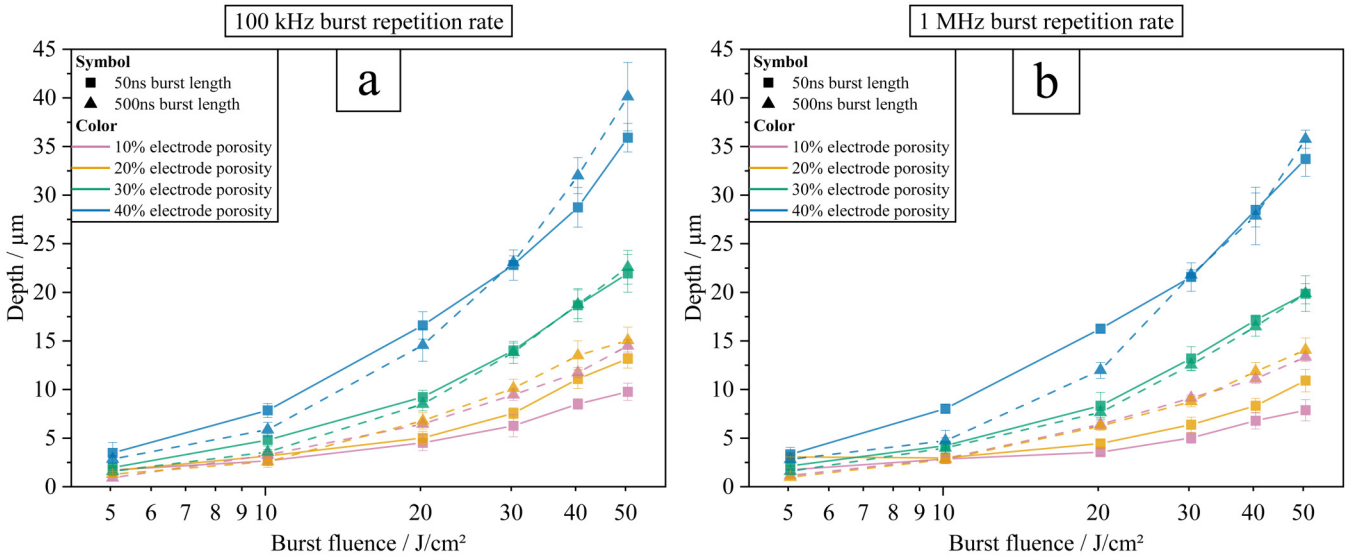

FIG. 7. Ablated depth as a function of burst fluence (F_{burst}) with a burst repetition rate ($f_{rep,burst}$) of 100 kHz (a) and 1 MHz (b) and values for 50 ns (square) and 500 ns (triangle) burst length (τ_{burst}) as well as 40% (blue), 30% (green), 20% (orange), and 10% (purple) porosity.

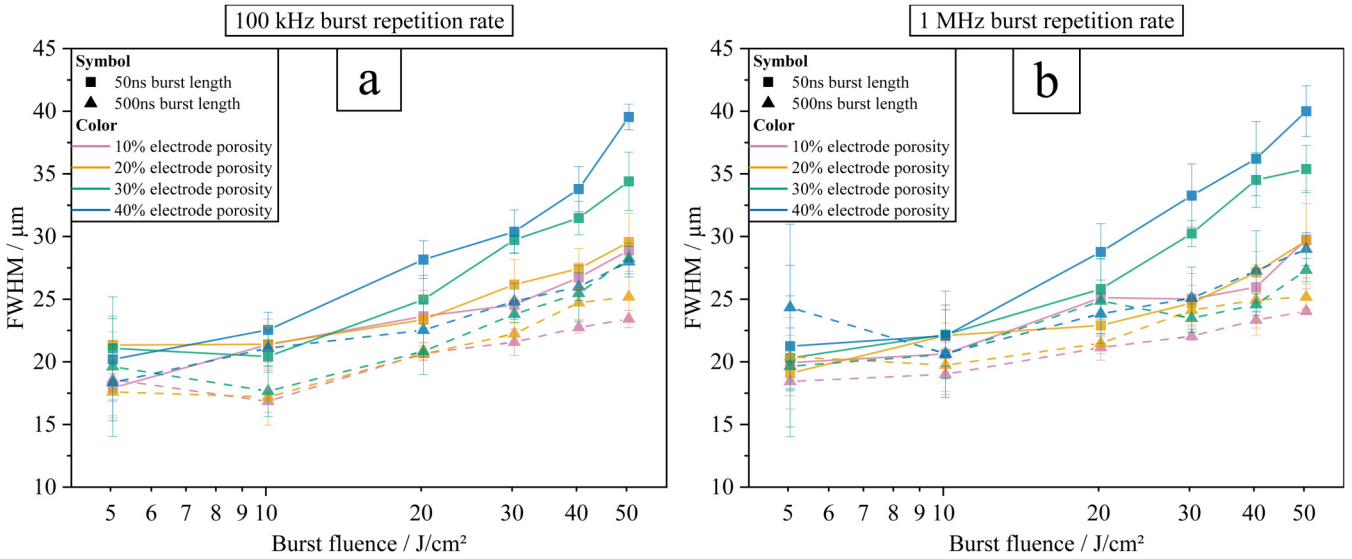

FIG. 8. FWHM of ablated channels as a function of burst fluence (F_{burst}) with a burst repetition rate ($f_{rep,burst}$) of 100 kHz (a) and 1 MHz (b) and values for 50 ns (square) and 500 ns (triangle) burst length (τ_{burst}) as well as 40% (blue), 30% (green), 20% (orange), and 10% (purple) porosity.

value at 5.1 J/cm^2 is likely to be caused by the aforementioned ablation threshold. By comparing Fig. 8(a) with Fig. 8(b), no significant difference in trend is observed.

Furthermore, when comparing the results from Figs. 4–8 and Fig. 9, the impact of the burst repetition rate can now be analyzed more specifically. In Fig. 9(a), the ablation efficiency, and in Fig. 9(b), the FWHM are plotted for the highest porosity (blue) and the lowest (purple), in order to highlight the most significant difference. This clarifies that, when the pulse-to-pulse distances are kept constant, the impact of the burst repetition rate on the ablated area, ablation

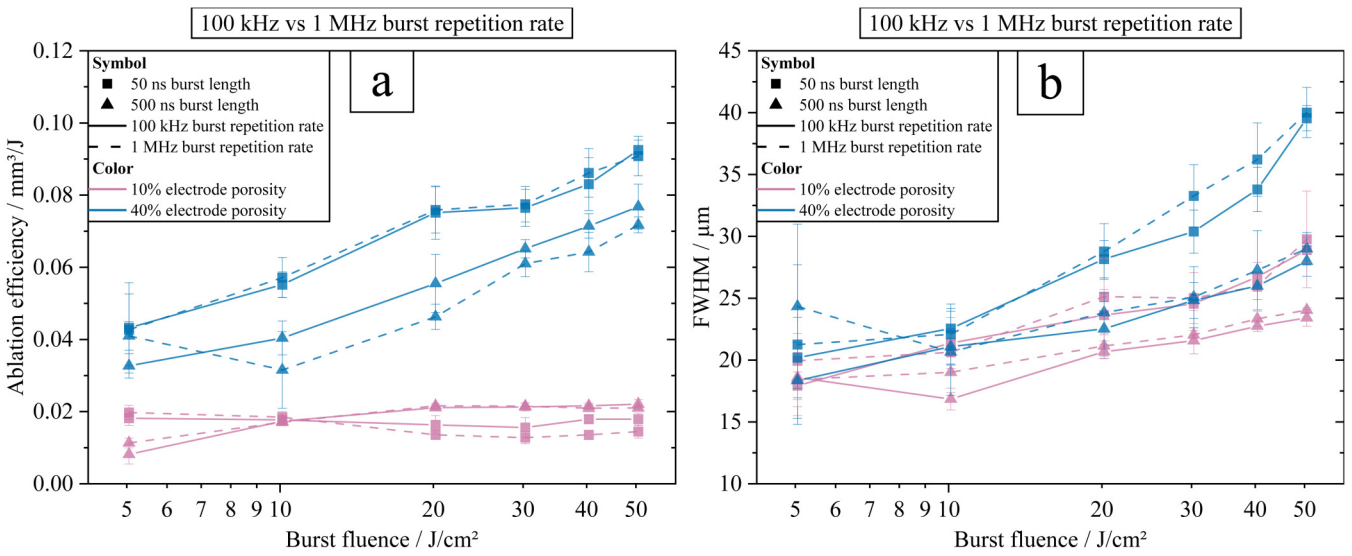

FIG. 9. Laser ablation efficiency (*Eff*) (a) and FWHM of ablated channels (b) as a function of burst fluence (F_{burst}) with a burst repetition rate ($f_{rep,burst}$) of 100 kHz and 1 MHz and values for 50 ns (square) and 500 ns (triangle) burst length (τ_{burst}) as well as 40% (blue) and 10% (purple) porosity.

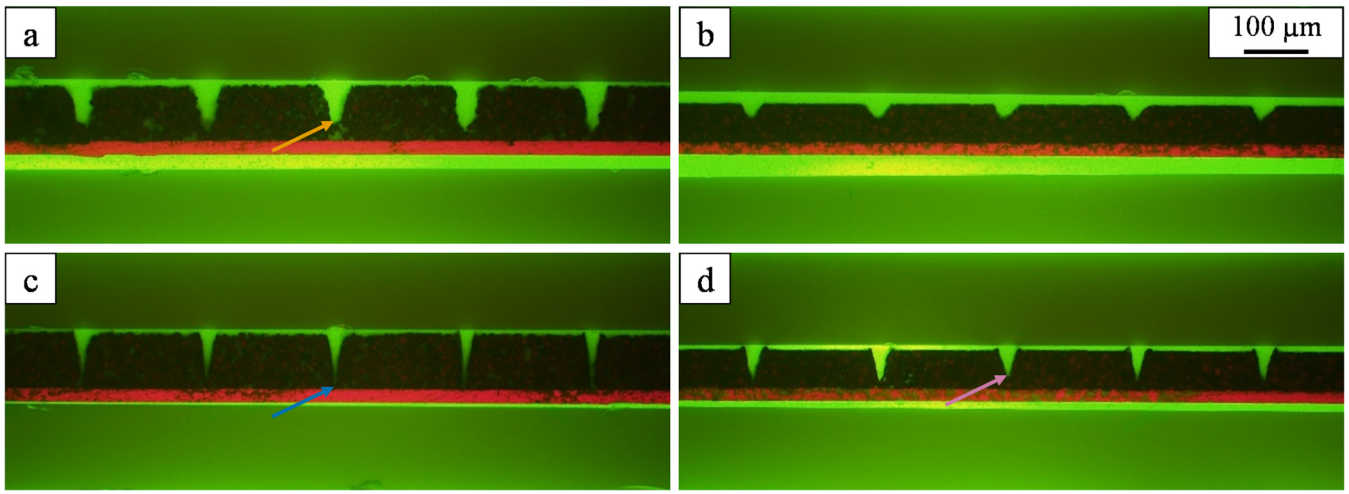

FIG. 10. Cross-sectional view of laser-structured NMC 811 electrodes with a porosity of 40% as shown in (a) and (c), as well as those with 10% porosity exhibited in (b) and (d). A burst fluence (F_{burst}) of 20.2 J/cm^2 and a burst length (τ_{burst}) of 50 ns were used for the structuring of electrodes shown in (a) and (b), while a burst length of 500 ns was applied for the structuring of electrodes in (c) and (d). Increased ablation rate is marked with an orange arrow, slightly deeper ablation with a blue arrow, and significantly deeper ablation with a purple arrow.

efficiency, and *aspect ratio* is minimal. However, the burst length and the average laser power (burst fluence) have a much stronger impact on the laser ablation process.

An optimal set of process parameters generally depends on the specific application. However, for the on-site scenario investigated here, a suitable compromise between laser ablation efficiency and resulting channel geometry was found at a burst fluence of 20.2 J/cm^2 and a burst repetition rate of 1 MHz.

To better understand the influence of ablation depth and scan repetition, additional samples were prepared using these parameters in combination with burst lengths of 50 and 500 ns, as well as electrodes with the highest and lowest porosity (40% and 10%), as shown in Fig. 10 with cross-sectional images using an optical magnification of 16. These porosities were used to maximize the observable differences in the ablation. The accumulated burst energy for all four parameter sets was again kept constant, using the same number of repetitions. The number of repetitions was chosen as the lowest number of repetitions among the four variants (two burst lengths and two porosities) required to reach the current collector. Figure 10(c) shows the corresponding channels reaching the current collector after 24 scan repetitions, with a burst length of 500 ns and an electrode porosity of 40%.

In agreement with the results from Fig. 4, at higher porosities [Figs. 10(a) and 10(c)], the shorter burst length [Fig. 10(a)] resulted in an increased ablation rate (ablated area), as marked with the orange arrow, whereas at lower porosities [Figs. 10(b) and 10(d)], the longer burst length [Fig. 10(d)] led to an increased material removal rate. The results also show a similar trend to Fig. 7, where the ablation depth increases with higher porosity [Fig. 10(a) and 10(b)]. In addition, they show a clear dependence of ablation depth on burst length, since the channels with longer bursts in Fig. 10(c) are slightly deeper, as marked with the blue arrow, and those in Fig. 10(d) significantly deeper, as marked with the purple arrow, than their respective comparison with shorter bursts [Figs. 10(a) and 10(b)]. This primarily contributes to the high *aspect ratio* observed with higher burst lengths through an increase in ablated depth in comparison to the high *aspect ratio* achieved by a reduction of ablated FWHM using low (three) scan repetitions as shown in Fig. 6. Consistent with Fig. 8, longer burst lengths [Figs. 10(c) and 10(d)] lead to a decrease in FWHM, especially for higher porosities [Fig. 10(c)].

In addition, top-view images were prepared using a scanning electron microscope (SEM, Phenom XL PW-100-018, Thermo Fisher Scientific Inc., Waltham, USA) at 10 kV accelerating voltage and a magnification of 5000 with a secondary electron detector, as shown in Fig. 11. The SEM images provide more insight into the effect of the laser ablation process on the electrode materials. At higher electrode porosities [Figs. 11(a) and 11(c)], more material was removed in comparison to electrodes with lower porosity [Figs. 11(b) and 11(d)], which is visible by the ablation depths. More pronounced differences appear on the near-channel surface regions. For shorter burst lengths [Figs. 11(a) and 11(b)], the surface mainly consisted of relatively large particles (likely NMC 811) that appeared less connected by binder, as marked with blue arrows. In addition, only minor modifications of the particle surfaces are visible, as marked with green arrows. In contrast, laser structuring of NMC 811 electrodes using a longer burst length [Figs. 11(c) and 11(d)] showed higher ablation depths, as marked with orange arrows, and a more homogeneous, layer-like surface, as marked with purple arrows. This suggests that for laser structuring with the shorter 50 ns burst length, the ablation process is consistent with being mainly dominated by selective binder removal, likely due to the higher single-pulse fluence resulting from fewer pulses per burst at the same average power. For laser ablation with the longer burst length of 500 ns, there was likely an additional

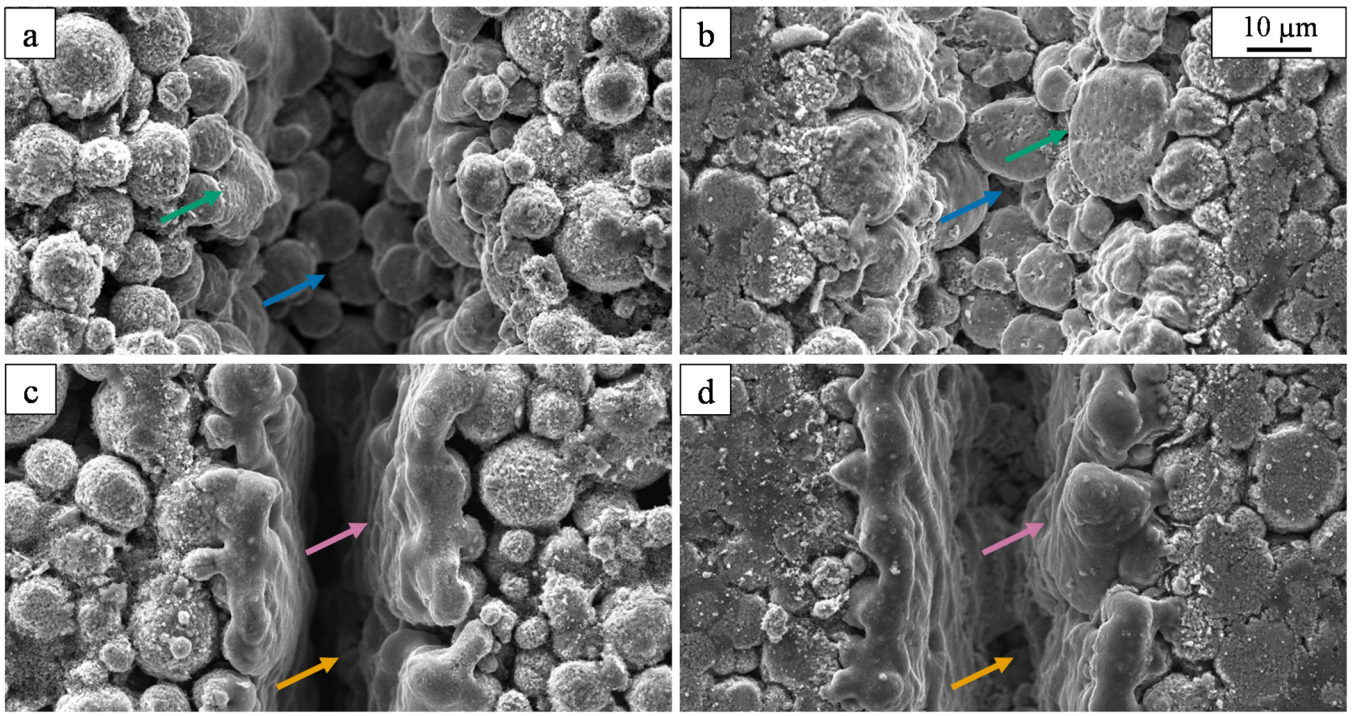

FIG. 11. Top view of the laser-structured NMC 811 electrodes with a porosity of 40% as shown in (a) and (c), as well as those with a 10% porosity shown in (b) and (d). A burst fluence (F_{burst}) of 20.2 J/cm^2 and a burst length (τ_{burst}) of 50 ns were applied for the structuring of NMC 811 cathodes shown in (a) and (b), while a burst length of 500 ns was applied for the structuring of ones in (c) and (d). Particles less connected by binder marked with blue arrows, minor particle modification marked with green arrows, higher ablation depths marked with orange arrows, and homogeneous, layer-like surface marked with purple arrows.

temperature-driven contribution. The longer bursts likely lead to cumulative heating of the laser-induced plasma plume due to the higher number of pulses, which can result in increased temperatures in near-channel surface regions. The high *aspect ratio* of the generated channels also enhances the probability of plasma–material interaction, which may contribute to increased temperatures in near-channel surface regions, as indicated by surface features consistent with resolidified or modified active material [Figs. 11(c) and 11(d)].

Based on the presented data, an idealized *processing rate* (cm^2/s) is introduced and determined by the scan speed, the pitch, and the scan repetitions, using Eq. (5). This equation does not consider process-slowing effects such as scanner jump times,

$$\text{Processing rate} = \frac{v_{\text{scan}} \cdot x_{\text{pitch}}}{n_{\text{scan,total}}}. \tag{5}$$

For the overall most promising setup 4 of Table II (burst length 500 ns, burst repetition rate 1 MHz, scan speed 20 m/s), a burst fluence of 20.2 J/cm^2 and a pitch distance of 200 μm result in a *processing rate* of 1.67 cm^2/s. One possible approach for further upscaling is the use of the maximum available laser power with the same burst fluence using a beam splitter (multibeam approach). Even when considering optical losses (ca. 10%) in the beam path and the splitter, a 1 × 10 beam splitter likely provides sufficient power per beam. This would increase the *processing rate* up to approximately 16.67 cm^2/s. By using an even higher laser power of up to 1 kW in combination with a 1 × 22 beam splitter, the system would still provide sufficient power per beam for a processing rate of up to 36.67 cm^2/s.

IV. CONCLUSIONS

Establishing the 3D battery concept by laser ablation of composite electrodes with GHz bursts is a very promising approach to further enhance the performance of LIBs. This work investigated the laser ablation of NMC 811 cathodes with different porosities using varying burst fluences and burst lengths with a GHz burst high-power laser.

Distinct ablation characteristics were observed depending on electrode porosity and burst length, showing clear trends in the interplay between these parameters. Shorter bursts significantly increased the ablation efficiency for electrodes with higher porosities, while for electrodes with lower porosities, the ablation efficiency increased with longer bursts. Both effects can be further enhanced by increasing the burst fluence within the investigated range from 5.1 to 50.5 J/cm^2. In addition, longer bursts resulted in channel geometries with an increasing *aspect ratio*. This trend is mainly influenced by a reduction in the ablated FWHM using a low number of scan repetitions and by an increase in the ablated

depth using a high number of scan repetitions. The ablated depth increases especially for electrodes with lower porosities and for longer bursts. The variation of repetition rates from 100 kHz to 1 MHz at identical burst energies showed only a minor influence on the ablation behavior of NMC 811 cathodes.

Further insights from cross-sectional analyses and SEM images showed that, while the general trends in ablation depth and geometry remain consistent, clear differences in surface morphology occur. Shorter burst lengths mainly lead to surfaces consisting of relatively large particles (likely NMC 811) with only minor visible modification, which is consistent with the ablation process being dominated by selective binder removal. In contrast, longer burst lengths result in a more homogeneous, layer-like surface structure, suggesting an additional temperature-driven contribution. This is likely caused by enhanced plasma–material interaction, which may lead to increased temperatures in near-channel surface regions and correspondingly stronger material modification.

Overall, longer burst lengths show a beneficial effect, particularly for low-porosity electrodes, not only in terms of ablation efficiency but also with respect to achievable channel geometry and aspect ratio. For the most promising parameter set (burst length 500 ns, burst repetition rate 1 MHz, scan speed 20 m/s) at a burst fluence of 20.2 J/cm^2 and a pitch distance of 200 μm, a *processing rate* of 1.67 cm^2/s was achieved. In addition, the results show a strong potential for upscaling. The use of higher laser power of up to 1 kW in combination with beam splitting would allow a significant increase in throughput. Even when considering optical losses, a 1 × 22 beam splitter would still provide sufficient power per beam and enable a *processing rate* of up to 36.67 cm^2/s.

Future work will include the investigation of higher burst fluences, different burst lengths, and repetition rates, as well as NMC 811 cathodes with varying binder systems and active material particle sizes. Furthermore, the impact of laser structuring on the electrode material, such as temperature-related phase transitions or the re-deposition of conductive additives, will be analyzed. Additional electrochemical investigations will also be performed.

ACKNOWLEDGMENTS

We are grateful to our colleagues Viktoria Falkowski, Yannic Sterzl, Alexandra Reif, and Heino Besser for their support during laser processing and analytics. This research has received funding from the European Union's Horizon Europe Research and Innovation Program under Grant Agreement Nos. 101069705 and 101086227.

AUTHOR DECLARATIONS

Conflict of Interest

The authors have no conflicts to disclose.

Author Contributions

Niclas Straßburger: Conceptualization (lead); Data curation (lead); Formal analysis (lead); Investigation (lead); Methodology (lead); Validation (lead); Visualization (lead); Writing – original draft (lead). **Penghui Zhu:** Conceptualization (supporting); Investigation (supporting); Writing – review & editing (supporting). **Wilhelm Pfleging:** Conceptualization (supporting); Funding acquisition (lead); Project administration (lead); Supervision (lead); Visualization (supporting); Writing – review & editing (lead).

DATA AVAILABILITY

The data that support the findings of this study are available from the corresponding author upon reasonable request.

REFERENCES

[1]M. Armand *et al.*, "Lithium-ion batteries—Current state of the art and anticipated developments," J. Power Sources **479**, 228708 (2020).
[2]W. Jin, H. Cha, S. Choi, and G. Song, "Electrode-level strategies for high-Ni cathodes in high-energy-density batteries beyond material design," Energy Mater. **5**, 500130 (2025).
[3]T. Hettesheimer *et al.*, *Lithium-Ion Battery Roadmap—Industrialization Perspectives Toward 2030* (Fraunhofer Institute for Systems and Innovation Research ISI, Karlsruhe, 2023).
[4]W. Liu, T. Placke, and K. T. Chau, "Overview of batteries and battery management for electric vehicles," Energy Rep. **8**, 4058–4084 (2022).
[5]W. Pfleging, "Recent progress in laser texturing of battery materials: A review of tuning electrochemical performances, related material development, and prospects for large-scale manufacturing," Int. J. Extreme Manuf. **3**, 012002 (2021).
[6]K.-H. Chen *et al.*, "Efficient fast-charging of lithium-ion batteries enabled by laser-patterned three-dimensional graphite anode architectures," J. Power Sources **471**, 228475 (2020).
[7]W. Pfleging, "3D electrode architectures for high energy and high power lithium-ion batteries," Proc. SPIE **12090**, 1209003 (2022).
[8]Z. Song, P. Zhu, W. Pfleging, and J. Sun, "Electrochemical performance of thick-film Li($Ni_{0.6}Mn_{0.2}Co_{0.2}$)O_2 cathode with hierarchic structures and laser ablation," Nanomaterials **11**, 2962 (2021).
[9]Y. Sterzl and W. Pfleging, "Optimizing structural patterns for 3D electrodes in lithium-ion batteries for enhanced fast-charging capability and reduced lithium plating," Batteries **10**, 160 (2024).
[10]N. Straßburger, P. Zhu, and W. Pfleging, "Hierarchical structuring of cathodes and anodes for lithium-ion batteries," Proc. SPIE **13005**, 130050B (2024).
[11]M. Park, Y. Gu, X. Mao, C. P. Grigoropoulos, and V. Zorba, "Mechanisms of ultrafast GHz burst fs laser ablation," Sci. Adv. **9**, eadf6397 (2023).
[12]N. Straßburger, P. Zhu, and W. Pfleging, "Gigahertz laser ablation of lithium nickel manganese cobalt oxide for lithium-ion batteries," Proc. SPIE **13351**, 1335104 (2025).
[13]C. Reinhold and W. Pfleging, "Ultrafast laser ablation of high-voltage cathodes using GHz burst mode operation," Proc. SPIE **13351**, 1335107 (2025).
[14]N. Straßburger, P. Zhu, and W. Pfleging, "GHz laser ablation of water-based NMC 811 electrodes: Optimizing pulse envelope shapes for enhanced manufacturing performance," Proc. SPIE **13881**, 1388107 (2026).
[15]M. Abdollahifar, H. Cavers, S. Scheffler, A. Diener, M. Lippke, and A. Kwade, "Insights into influencing electrode calendering on the battery performance," Adv. Energy Mater. **13**, 2300973 (2023).
[16]E. N. Primo, M. Chouchane, M. Touzin, P. Vazquez, and A. A. Franco, "Understanding the calendering processability of Li($Ni_{0.33}Mn_{0.33}Co_{0.33}$)$O_2$-based cathodes," J. Power Sources **488**, 229361 (2021).
[17]H. Zheng, L. Tan, G. Liu, X. Song, and V. S. Battaglia, "Calendering effects on the physical and electrochemical properties of Li[$Ni_{1/3}Mn_{1/3}Co_{1/3}$]O_2 cathode," J. Power Sources **208**, 52–57 (2012).
[18]Y. Sheng, C. R. Fell, Y. K. Son, B. M. Metz, J. Jiang, and B. C. Church, "Effect of calendering on electrode wettability in lithium-ion batteries," Front. Energy Res. **2**, 56 (2014).
[19]R. Ledesma, J. Fitz-Gerald, F. Palmieri, and J. Connell, "Determination of cross-sectional area of focused picosecond Gaussian laser beam" (NASA Langley Research Center, Hampton, VA, 2018).
[20]P. Zhu, H. J. Seifert, and W. Pfleging, "The ultrafast laser ablation of Li($Ni_{0.6}Mn_{0.2}Co_{0.2}$)O_2 electrodes with high mass loading," Appl. Sci. **9**, 4067 (2019).